AIAA 99-0092

Effects of Simulated-Spanwise-Ice Shapes on Airfoils: Experimental Investigation

S. Lee and M.B. Bragg
University of Illinois
Urbana, IL

37th AIAA Aerospace Sciences Meetings & Exhibit

11–14 January 1999/Reno,NV

EFFECTS OF SIMULATED-SPANWISE-ICE SHAPES ON AIRFOILS: EXPERIMENTAL INVESTIGATION

Sam Lee* and Michael B. Bragg+
University of Illinois at Urbana-Champaign, Urbana, IL 61801

ABSTRACT

An experimental investigation was conducted to determine the effect of simulated-spanwise-ice shapes on airfoil aerodynamics. The simulated ice shapes were tested on the NACA 23012 and the NLF 0414 airfoils at Re = 1.8 million. The ice shapes produced very different results on the two airfoils. The effects of the simulated ice shapes were much more severe on the NACA 23012, with a $C_{l,max}$ as low as 0.25 for the ice shape with a height to chord ratio of 0.0139. The lowest $C_{l,max}$ measured for the NLF 0414 with same ice shape was 0.68. The effect of the simulated ice shape on the flap hinge moment was much more severe on the NACA 23012 than on the NLF 0414. The NACA 23012 effects were more severe due to the large adverse pressure gradients at the ice-shape location. Various simulated ice shape size and geometries were investigated on the NACA 23012. The aerodynamic penalties (in C_l, C_d, C_m, and C_h) became more severe as the height to chord ratio of the simulated ice shape was increased from 0.0056 to 0.0139. The variations in the simulated ice shape geometry also had measurable effects on the airfoil aerodynamics.

NOMENCLATURE

C_d	Drag coefficient
C_h	Flap hinge moment coefficient
$C_{h,\alpha}$	Flap hinge moment curve slope
C_l	Lift coefficient
$C_{l,max}$	Maximum lift coefficient
$C_{l,\alpha}$	Lift curve slope
C_m	Pitching moment coefficient
C_p	Pressure coefficient
$C_{p,min}$	Minimum pressure coefficient
Re	Reynolds number
c	Model chord
k	Protuberance height
x	Model coordinate in chordwise direction
α	Angle of attack

INTRODUCTION

A spanwise-step type of ice accretion protuberance can occur on an aircraft wing when ice accretes behind the leading-edge de-icing system.[1] This type of accretion presents both a forward and aft facing step to the flow and is essentially 2-D, extending spanwise on the wing. They generally occurs in the presence of supercooled large droplets (SLD), where the droplet sizes are much larger than those in the FAA Part 25, Appendix C icing envelopes. This type of accretion can lead to large changes in the lateral control (and the associated aileron hinge moments) by severely altering the flow over the ailerons. This is thought to have caused the crash of an ATR-72 commuter aircraft near Roselawn, Indiana on October 31, 1994.[2] A spanwise-step type of ice accretion can also occur in supercooled droplet clouds, of Appendix C size, at air temperatures near freezing. This occurs when the surface water runs back and freezes behind the leading-edge deicing system.

A recent study at the University of Wyoming, which examined the effects of various types of icing conditions on a King Air aircraft, found that the freezing drizzle exposure resulted in the most severe performance degradation.[3] Under this icing condition, a spanwise step ice accretion was observed. In low-Reynolds number wind tunnel tests with simulated ice shapes, Ashenden, Lindberg and Marwitz[4] found that a freezing drizzle ice shape with a simulated de-icing boot operation resulted in a more severe performance

* Graduate Research Assistant, Department of Aeronautical and Astronautical Engineering, Student Member AIAA
+ Professor, Department of Aeronautical and Astronautical Engineering, Associate Fellow AIAA

degradation than one without the de-icing boot operation. When the de-icing boot is not in use (in SLD icing condition), the ice accretion occurs around the leading edge of the wing and tends to conform to the geometry of the wing. No spanwise step is formed. However, when the de-icing system is in use, the spanwise-step shape forms immediately downstream of the boot, which typically extends to 5 - 10% chord on the upper surface.

In 1996 Bragg[5,6] reviewed the aerodynamic effects of the SLD ice accretion and showed that the SLD accretion not only degraded lift and drag, but also adversely affected the aileron hinge moment. This was thought to be the result of a large separation bubble that formed downtream of the accretion, which severely altered the pressure distribution over the aileron. Bragg reviewed NACA data on airfoils with 2-D protuberances to provide a useful background. In 1932, Jacobs[7] tested a series of protuberances of different heights at various chordwise locations on a NACA 0012 airfoil. The test revealed that the 5% and 15% chord locations on the airfoil upper surface were the most critical in terms of lift and drag penalties for the large protuberance (k/c = 0.0125). This protuberance resulted in reductions in lift as much by as 68%, and a large change in the pitching moment. However, no locations between 5 and 15% were tested. For smaller protuberances, (k/c < 0.005), the effects were much less severe, and the most critical location was the leading edge.

In 1956, Bowden[8] tested a spanwise spoiler-type step protuberance of k/c = 0.00286 and 0.00572 on a NACA 0011 airfoil at x/c = 0.01, 0.025, and 0.05. The test showed that the effects of the protuberance on lift and pitching moment became more severe as it was moved closer to the leading edge. The reduction in lift was as high as 25%. At angles of attack greater than 4°, the maximum increase in the drag was observed to occur when the protuberance was placed near the location of maximum local velocity. Calay, Holdo and Mayman[9] tested 3 different small simulated runback ice shapes (k/c = 0.0035) at 5, 15 and 25% chord on a NACA 0012 airfoil. The shapes at 5% chord had the largest effect on lift and drag, with penalties similar to those seen by Bowden.[8] The reports described do not provide the reasons why one protuberance size, shape, and location produced a more severe degradation in aerodynamic performance and control than another. This may have been due to the limited scope of the work that did not provide the authors enough information to draw any definitive conclusions.

In 1998, Lee, et al.[10] presented the initial findings of a comprehensive experimental and computational study of the aerodynamic effects of simulated SLD ice shapes with k/c values of 0.0083 and 0.0139. The study examined the sensitivity of airfoil lift, drag, pitching moment, and flap hinge moment to different chordwise locations and size of the ice simulations. They found the most critical simulated ice shape location on the NACA 23012 airfoil to be x/c = 0.12 for k/c = 0.0139, with a $C_{l,max}$ of 0.27. This was a reduction of more than 80% when compared to the clean airfoil. The primary cause of this reduction in lift was the long separation bubble that formed downstream of the simulated ice shape. This prevented the leading-edge suction (where most of the lift on the clean model was generated) from forming and led to early stall. The computational results compared well to the experimental results and consistently predicted all of the major trends of the aerodynamic features that were measured experimentally. This comparison provided a good validation of both the experimental and computational results.

The current report is the continuation of the experimental component of the study first presented by Lee, et al.[10] The current computational work has been reported by Dunn and Loth.[11] In the current experimental paper, the effect of simulated ice shape size and geometry on airfoil aerodynamics was investigated. Also, the importance of airfoil geometry on iced-airfoil aerodynamics was investigated by testing the simulated ice shapes on the NLF 0414 airfoil, which has aerodynamic characteristics quite different from the NACA 23012. Studying the effect of simulated ice shapes on two very different airfoils provided a much clearer explanation of the aerodynamic factors that determine the critical ice shape location.

EXPERIMENTAL METHODS

The tests were performed in the University of Illinois 3'x4' Subsonic Wind Tunnel. Two 18-inch chord airfoil models were used: a modified NACA 23012 model (described in more detail in Lee, et al.[10]) and a NLF 0414 model. A 25% chord simple flap was present on both of the model. The NACA 23012 airfoil was chosen because it has aerodynamic characteristics that are typical of the current commuter aircraft fleet. The NLF 0414 airfoil was chosen because, as a natural laminar flow airfoil, it has aerodynamic characteristics that are quite different from the NACA 23012. The differences will be explained in more detail in the next section.

Figure 1 is a schematic of the experimental setup. The leading edge of the flap was located at x/c = 0.75, and the flap hinge axis was located at x/c = 0.779. The

model was attached to a three-component balance, which was also used to set the angle of attack. The flap was actuated by a two-arm linkage system, which was driven by a linear traverse. The traverse was mounted on the metric force plate of the balance. A load cell was attached in one of the arms of the flap actuation linkage and measured the flap hinge moment. The NACA 23012 model had 50 surface pressure taps on the main element and 30 on the flap (including 12 spanwise taps). The NLF 0414 model had 59 surface pressure taps on the main element and 22 taps on the flap. A traverseable wake rake with 59 total-pressure probes was used to measure the wake pressures from which the drag was determined. The pressures were measured using an electronically scanned pressure (ESP) system.

The lift coefficient (C_l) and pitching moment coefficient (C_m) measurements were derived from both the force balance and the surface pressure measurements. In this report, only C_l and C_m data from the pressure measurements will be shown. The primary drag coefficient (C_d) measurements were taken with the wake rake and confirmed with the force balance. The flap hinge moment coefficients (C_h) were measured with the flap hinge load cell and confirmed with the surface pressure measurements. The surface pressure measurements and fluorescent oil flow visualization were used for flow diagnostics. The C_l, C_m, and C_d measurements were calculated using standard methods with conventional definitions. The C_h was obtained by determining the trailing-edge-down moment about the flap hinge line and nondimensionalizing by the flap surface area and the flap chord length. All of the aerodynamic coefficients were corrected for wall effects using the method described by Rae and Pope.[12]

The baseline SLD ice accretions were simulated with wooden forward-facing quarter-round shapes of 0.10", 0.15", and 0.25". This is shown in Fig. 2. The other geometries tested consisted of backward facing quarter round, half-round, and forward-facing ramp, (all with 0.25" height) as shown in Fig. 3. The ramp shape had a base length to height ratio of 3.

Roughness was also used in place of and in addition to the simulated ice shape. When it was used in place of the ice shape, the roughness had a 0.5" chordwise extent. When used with the ice shape, the roughness extended upstream and/or downstream from the ice shape. The chordwise extent of the upstream roughness varied from 0.25" to 2", and the extent of the downstream roughness was 2". The roughness was simulated using 16-grit aluminum carbide attached to a double-sided tape. This resulted in 0.025" roughness height, with k/c = 0.0014. The roughness density was estimated to be about 30%.

For selected cases, the boundary layer was tripped at x/c = 0.02 on the upper surface and at x/c = 0.05 on the lower surface. The trip consisted of 0.012-inch diameter microbeads that were applied onto a 0.003 inch thick and 0.25 inch wide double-sided tape.

The flap gap was sealed on the lower surface using a 1" wide Mylar strip that was taped only on the main element side. At positive angles of attack, the high pressure on the lower surface of the model pushed the Mylar strip against the flap gap, effectively sealing it without adversely affecting the measurements from the flap hinge balance.

All measurements were taken at 50 Hz and averaged over 2 seconds. The force balance data were low-pass filtered at 1Hz. None of the other measurements were filtered. A typical run consisted of sweeping the angle of attack from negative stall to a few degrees past positive stall in 1° increments.

Shown in Table 1 are the uncertainty estimates of the aerodynamic coefficients for a typical data point. The case shown is that of the clean the NACA 23012 model at $\alpha = 5^o$ with zero flap deflection and Re = 1.8 million. The relative uncertainties for C_m and C_h appear to be rather large, but this was due to relatively small reference values at this point. The clean model baseline measurements on the NACA 23012 compared favorably with the previously published experimental measurements of Stuttgart.[13]

RESULTS AND DISCUSSION

In this section, the comparisons of iced-airfoil aerodynamics between the NACA 23012 and NLF 0414 airfoils will be presented. This will be followed by the effect of simulated ice shape size and geometry on the NACA 23012 airfoil.

Comparisons between NACA 23012 and NLF 0414

Large differences in the iced-airfoil aerodynamics between the NACA 23012 and the NLF 0414 were observed. This was because these two airfoils have very different geometry and aerodynamic characteristics. Figure 4 shows the comparisons between the NACA 23012 and the NLF 0414 geometry. The NACA 23012 is a thinner (t/c_{max} = 0.12) airfoil, with its maximum thickness at x/c = 0.30. The NLF 0414 (t/c_{max} = 0.14) has nearly uniform thickness from x/c = 0.10 to 0.70 and is highly cambered near the trailing edge. NACA 23012 was designed to provide low pitching moment by generating most of the lift near the leading edge. NLF 0414, however, was designed to achieve a laminar flow over the airfoil by distributing the load over a large portion of the chord and delaying

the onset of pressure recovery and the accompanying large adverse pressure gradient (where transition occurs) until around 70% chord.

The different aerodynamic characteristics are quite apparent in the measured clean-model surface pressure of Fig. 5. In this figure, the surface pressures are compared at nearly identical lift coefficients. However, because the NLF 0414 is highly cambered, it's α was much lower than that of NACA 23012. On both of the models, there was a pressure discontinuity near x/c = 0.76 due to the flap gap. On the NACA 23012, there is a strong suction peak centered at x/c =0.08, followed by an adverse pressure gradient that extended to the trailing edge. There is a discontinuity in the surface pressures between x/c = 0.18 and 0.20 on the upper surface due to a laminar separation bubble. The flow was laminar upstream of this location and turbulent downstream of this location. On the NLF 0414, a leading-edge suction peak was not present. Instead, after the initial acceleration around the leading edge to x/c = 0.02, the surface pressure was nearly constant ($C_p \approx -0.8$) to x/c = 0.73. The pressure recovery process began at this point and the adverse pressure gradient extended from here to the trailing edge. Since the flow around the nose on the NACA 23012 accelerated to a $C_{p,min} = -1.7$ versus only -0.9 for the NLF 0414, much more pressure recovery was required on the NACA 23012 airfoil.

Because the adverse pressure gradient did not start until x/c = 0.73, the flow was laminar over the first 75% of the chord (this was verified by flow visualization), compared to 18% chord on NACA 23012. A result of this is a lower drag because such a large percentage of the model was under laminar flow. However, this comes at a cost of much higher pitching moment. Because of the large region of constant pressure, the lift was distributed much more uniformly over the entire length of the chord, resulting in a large pitching moment about the quarter chord. The NACA 23012 was much more front loaded, resulting in a low pitching moment about the quarter chord.

Effect of Ice-Shape Locations on NACA 23012 and NLF 0414

All of the results shown in this section were with a 0.25" forward-facing quarter round ice shape simulation. The boundary layer was tripped at x/c = 0.02 on the upper surface and x/c = 0.05 on the lower surface. The boundary layer was not tripped for the clean model or when the ice shape was located at $x/c \leq 0.02$. The Reynolds number was 1.8 million.

The differences in the airfoil geometry (and the resulting clean-airfoil aerodynamic characteristics) between the NACA 23012 and NLF 0414 led to large differences in behavior with simulated ice shapes. Figure 6 shows the effect of simulated ice shape on the lift of the two airfoils. Varying the ice shape location form x/c = 0.02 to 0.20 had large effects on lift on NACA 23012 (Fig. 6a). The loss in lift was most severe when the ice shape was located at x/c = 0.10 (with $C_{l,max} = 0.27$). When the ice shape was located at x/c = 0.02 $C_{l,max}$ was approximately doubled. A classical $C_{l,max}$, where as α is increased C_l eventually reaches a maximum and then decreases, was not observed when the simulated ice shape was located at x/c = 0.20. Instead, only an inflection in the curve was observed at $\alpha = 4°$ (and $C_l = 0.42$). Jacobs[7] observed similar lift curves (where a real $C_{l,max}$ was not observed) under certain conditions. However, the location of this inflection is effectively the $C_{l,max}$ because the surface pressure measurements showed that it was caused by the flow downstream of the simulated ice shape completely separating off the airfoil even though the flow upstream of the simulated ice shape was still attached. The increase in the airfoil drag was large in the angle of attack range where the inflection in the lift curve was observed. This further supports representing this as the $C_{l,max}$.

Figure 6b shows the effect of simulated ice on the lift of the NLF 0414. When the simulated ice shape location was varied from x/c = 0.02 to 0.20, the lift curves did not vary significantly, with only slight changes in the $C_{l,max}$ and α_{stall}. The maximum lift was also much higher than on the NACA 23012, with a typical value of 0.70. When the ice shape was located at x/c = 0.40, the lift curve was significantly different (and similar to the NACA 23012 with the simulated ice at x/c = 0.20). A normal $C_{l,max}$ was not observed, and only an inflection in the curve was observed at $\alpha = 1°$ (and $C_l = 0.20$).

The large differences between the NACA 23012 and NLF 0414 airfoils can also be seen in Fig. 7, a summary of $C_{l,max}$ as a function of ice shape location. The lowest $C_{l,max}$ for the NACA 23012 was 0.25 (an 83% reduction from the clean value) when the simulated ice shape was located at x/c = 0.12. The maximum lift increased rapidly as the simulated ice was moved upstream and downstream of this location. Figure 7 shows that on the NLF 0414, the variations in the ice-shape location did not have a large effect on $C_{l,max}$ between x/c = 0.02 and x/c = 0.20. The $C_{l,max}$ varied only between 0.68 and 0.79 when the ice shape was located in this region. These values were much higher than those observed for the NACA 23012. Figure 7 shows that on the NLF 0414, there was a rapid decrease in the $C_{l,max}$ downstream of x/c = 0.20. However, what is shown is the C_l value at the inflection in the lift curve since, as described previously, a

"classical" $C_{l,max}$ was not observed when the simulated ice shape was located at $x/c \geq 0.20$.

Very different results were observed for flap hinge moments, as Fig. 8 shows. On the NACA 23012 (Fig. 8a), the ice shape produced a significant change in the C_h curve (compared to the clean case) at all ice shape locations. There was rapid divergence of the flap hinge moment at a critical angle of attack at which it became sharply negative. This critical angle of attack varied from 1° (for x/c = 0.10 and 0.20) to 6° (for x/c = 0.02). The ice shape did not produce significant changes in the C_h values for the NLF 0414 when it was located between x/c = 0.02 and 0.20. However, the slope $C_{h,\alpha}$ was more negative at about $\alpha = 5°$, where the airfoil was stalling. When the ice shape was at x/c = 0.40, the C_h was significantly more negative (or flap up) than the clean case between $\alpha = -5°$ and 7°. At the other angles attack, the values did not vary by a large amount.

As stated in the Introduction, studies[7,8] have shown that the effects of spanwise surface protuberance (of k/c < 0.005) on lift, drag, and pitching moment became more severe as it was moved closer to the leading edge. Gregory and O'Reilly[14] showed that k/c = 0.0004 surface roughness resulted in the most severe loss in $C_{l,max}$ (on a NACA 0012 airfoil) when it was placed at the leading edge. Bowden[8] observed that the maximum increases in the drag occurred when the protuberance was located near the location of maximum local velocity (or minimum C_p). This is thought to be the case because the protuberance would extract the greatest amount of boundary-layer momentum at that location, which would thicken the boundary layer and increase drag.

Figure 9 shows ΔC_d, the drag increase due to the ice shape when compared to the clean airfoil, for the 0.25" ice shape. Each curve represents a fixed angle of attack, and the simulated ice shape location is depicted on the x-axis. Also shown on the figure by the solid arrows are the locations of maximum local air velocity (or $C_{p,min}$) of the clean airfoil for each angle of attack and the open arrows are the location of the maximum adverse pressure gradient (also of the clean airfoil). Figure 9a shows the drag increase on the NACA 23012. It shows that the most critical location (in terms of ΔC_d) moved upstream with increasing angles of attack and closely coincided with the location of the maximum local air velocity. This closely agreed with Bowden.[8]

Fig. 9b shows the drag increase on the NLF 0414. At angles of attack of -3° and 0°, a leading-edge suction peak was not observed. Instead, the highest local air velocity occurred near mid chord at x/c = 0.55 (for $\alpha = -3°$) and 0.45 (for $\alpha = 0°$). The location of maximum adverse pressure gradient was located at the trailing edge pressure recovery near x/c = 0.75. Because the simulated ice shape was not tested at x/c > 0.50, some of these points described above are not shown in Fig. 9b. At angles of attack of 3° and 5°, a leading edge suction peak was present, with the location of the $C_{p,min}$ at x/c = 0.01. The location of the maximum adverse pressure gradient was located immediately downstream of the $C_{P,min}$ and not at the trailing edge pressure recovery. At angles of attack of -3° and 0° (where there was no leading-edge suction peak on the clean model), there was a gradual increase in ΔC_d as the ice shape was moved downstream from the leading edge to x/c = 0.30. As the ice shape was moved further downstream, ΔC_d increased at a much faster rate. At angles of attack of 3° and 5°, ΔC_d was relatively constant between x/c = 0.02 and x/c = 0.20, after which ΔC_d started to increase rapidly. The ΔC_d values eventually reached a maximum (at x/c = 0.4 for $\alpha = 3°$ and at x/c = 0.35 for $\alpha = 5°$) after which they decreased. Unlike the NACA 23012, the location of the maximum local air velocity was not a good indicator of the most critical simulated ice-shape location.

Figure 10 shows the lift loss ΔC_l (when compared to the clean airfoil) due to the 0.25" ice shape simulation. On the NACA 23012 (Fig. 10a) the most critical location of the simulated ice shape (in terms of lift loss) was between x/c = 0.10 and 0.12 and did not vary significantly with angle of attack. This was the same location that resulted in the lowest $C_{l,max}$, as shown in Fig. 7. The most critical location was situated between the locations of the maximum local air velocity and the maximum adverse pressure gradient. Thus, it did appear that the most critical ice-shape location was related to these flow features.

The lift loss behavior of the NLF 0414 airfoil, as shown in Fig. 10b, was quite different from that of NACA 23012. Figure 10b shows that when the ice shape was placed between the leading edge and x/c = 0.20, there was not a large variation in the lift loss. This was similar to what was observed in the $C_{l,max}$ plot of Fig. 7. It was only when the ice shape was located downstream of x/c=0.30, and closer to the adverse pressure gradient at the trailing-edge pressure recovery that a much larger increase in the lift loss was observed. This was even the case at $\alpha = 3°$ and 5° where the adverse pressure gradient associated with the leading-edge suction peak was more severe than the trailing-edge pressure recovery. Unlike the NACA 23012, loss in lift increased with increasing chordwise location, and the locations of maximum local air velocity and adverse pressure gradient were not proper indicators for critical locations.

Flowfield Comparisons

The flowfield of the NACA 23012 and NLF 0414 airfoils will be discussed and compared in order to provide an explanation to the performance data of the previous section. Figure 11a shows the surface pressure distribution on the NACA 23012 model with the 0.25" simulated ice shape at various chordwise locations. The pressure distribution for the clean case shows a suction peak (C_p = -1.7) at x/c = 0.08. Well over half of the lift is centered on this large suction peak in the first 25% chord. When the simulated ice shape was present on the airfoil, a long separation bubble usually formed immediately downstream. A region of relatively constant pressure characterized this flow separation. The highest velocity on the airfoil usually occurs over this bubble because the flow accelerates over the ice shape before separating. Ahead of the ice shape, the C_p is much higher because the flow decelerates as it approaches the ice shape. The reattachment location can be estimated using a method proposed by Tani.[15] The bubble reattaches where the pressure in the perturbed flow (with ice shape) approaches the unperturbed flow (clean airfoil). However, this method only works for moderately long separation bubble. When the bubble is very long, the perturbed pressure never approaches the unperturbed pressure.

Fig 11a shows that when the simulated ice shape was at x/c = 0.02, the C_p in the separation bubble downstream of the simulated ice shape was even more negative than that of the clean model suction peak. The simulated ice shape was still located in a favorable pressure gradient, and the separation bubble was relatively short. This resulted in a surface pressure distribution that was not severely affected by the simulated ice shape.

When the simulated ice shape was located at and downstream of x/c = 0.10, a very long separation bubble formed downstream of the simulated ice shape. This was because the shape was located in an adverse pressure gradient. It was difficult to determine from the surface pressure values whether or not the separation bubble reattached. However, it was likely that at $\alpha = 5°$ the bubble was unsteady and was intermittently attached at the trailing edge. When the ice shape was located at x/c = 0.10, the large suction peak that normally forms near x/c = 0.08 was completely eliminated by this separation bubble. However, when the simulated ice shape was located downstream (x/c = 0.20 and 0.50), a significant suction peak was able to form ahead of the ice shape because there was a greater surface length for the flow to accelerate. This suction peak grew as the simulated ice shape was moved downstream. Thus, the most critical location (among the cases shown) was at x/c = 0.10. This was because upstream of this location, the simulated ice shape was located in a favorable pressure gradient, resulting in a short separation bubble. Downstream of this location, the ice shape was located far enough downstream that a significant leading-edge suction peak was able to form, recovering some of the lost lift.

On the clean model, the loading on the flap was very small, resulting in a very small value of C_h. For the cases where the separation bubble reached the flap, the flap became much more loaded, resulting in large changes in C_h. This can be seen in Fig. 8b.

Figure 11b shows the surface pressure distribution on the NLF 0414 model with the ice-shape simulation at various chordwise locations. The angle of attack was 1°, where the clean airfoil had a C_l similar to the NACA 23012 at $\alpha = 5°$. On the clean model, there was a sharp decrease in upper surface C_p from the leading edge to x/c = 0.06 as the flow accelerated around the leading edge of the model. The C_p then leveled off and was relatively constant between x/c = 0.10 and 0.70, providing the slightly favorable pressure gradient for laminar flow. The C_p then started to increase as the pressure recovery process started and continued until the trailing edge was reached. The lift was distributed relatively uniformly over the entire chord ahead of the pressure recovery, and there was no leading-edge suction peak.

When the ice shape was located at and between x/c = 0.02 and 0.20, low suction pressures were measured immediately downstream of the ice shape, which was caused by the acceleration of the flow over the ice shape and the separation bubble. The bubble reattached during a pressure recovery region, followed by a region of relatively constant C_p. The pressure then increased again as the flow recovered pressure approaching the trailing edge. When the ice shape was located between x/c = 0.02 and 0.20, the suction region (due to separation) had similar C_P values (-1.3) and the separation length did not vary as much as it did for the NACA 23012. The bubble length varied from 18% chord for x/c = 0.02 case to 28% chord for the x/c = 0.20 case. After the flow had reattached, the C_P on all three cases dropped to approximately 0.50 and remained fairly constant until the pressure recovery over the flap occurred.

When the ice shape was located at x/c = 0.40, the surface pressure distribution looked significantly different than those of the other three iced cases. The suction region downstream of the ice shape was at a higher pressure than the other cases, with a $C_{p,min}$ value of only -0.81. Also, based on the low trailing-edge pressures, it appears that the separation bubble may not have reattached, resulting in a separation length of 60%

chord. In the other three iced cases, the C_p values were very similar to the clean model values.

The reason for the similarities in the x/c = 0.02, 0.10, and 0.20 cases was that the ice shape and the resulting separation bubble was located in a region of relatively constant pressure (on the clean model). Thus, the separation bubbles in the three cases above were all allowed to attach in a similar pressure gradient (which happened to be nearly zero in this case). The resulting separation bubbles all appeared similar, with relatively similar suction regions and separation lengths because the ice shape was in a similar flowfield. The variation in the separation length may be due to the thicker boundary layer the ice shape encountered as it was moved downstream. The similarities ended when the ice shape was located at x/c = 0.40. Although the ice shape itself was in the region of constant pressure, it was located close to the clean model pressure recovery region (where there was a strong adverse pressure gradient). Thus, the separation bubble was forced to reattach in an adverse pressure gradient, resulting in a much longer bubble (or a trailing-edge separation).

At $\alpha = 1°$, the separation bubble did not reach the flap when the ice shape was located at and upstream of x/c = 0.20 (Fig. 11b). Thus, the pressure distributions over the flap were very similar, with similar C_h. When the ice shape was located at x/c = 0.40, the flow over the flap was separated and resulted in a large flap loading. This can be seen in Fig. 8b. On the clean NLF 0414 model, the flow over the flap was observed with flow visualization to stall at $\alpha = 5°$. Thus, the C_h - α curve with the ice shape at x/c = 0.40 converged with the clean case at $\alpha = 5°$ because the flow over the flap was separated for both of the cases.

Figure 12 shows the surface pressure comparison between the NACA 23012 and the NLF 0414 with the simulated ice shape at x/c = 0.10. The corrected angle of attack for the NACA 23012 was 4.93° and the corrected angle of attack for the NLF 0414 was 1.06°. If the simulated ice shapes were not attached to the models, these angles of attack would result in a C_l of approximately 0.60. However, with the ice shape, the C_l for the NACA 23012 was 0.25 and the C_l for NLF 0414 was 0.47. The reason the simulated ice shape has a much more severe effect on lift becomes quite apparent when one examines the surface pressure distributions. On the NACA 23012 model, the ice shape generated a much longer separation bubble because the simulated ice shape was located in a much more adverse pressure gradient. Although it was difficult to conclude from the surface pressures, it appeared that the separation bubble on the NACA 23012 had reached the region near the trailing edge, resulting in a near stall condition. The ice shape also effectively eliminated much of the leading edge-lift on the NACA 23012. The separation bubble was much shorter on the NLF 0414 model, having reattached near x/c = 0.35. Because of this, the momentum loss on the NLF 0414 was much less than that on the NACA 23012, resulting in much less drag. This also allowed a much stronger suction region to form downstream of the ice shape, resulting in greater lift. Although the ice shape eliminated almost all of the lift ahead of it, the increased lift in the bubble region immediately downstream made up nearly all of the lost lift. Also, because the separation bubble was still short, increasing α will result in a greater lift. On the NACA 23012, increasing α will result in only a marginal gain in lift because the model is at near stall condition.

Effect of Simulated Ice Size and Shape

Figure 13 shows the effect of the simulated ice shape size on lift and flap hinge moment of the NACA 23012. The height of the forward-facing quarter round was varied from 0.10" to 0.25" (k/c = 0.056 to 0.0139) and were tested on the airfoil surface at x/c = 0.10. The boundary layer was tripped. Figure 13a shows significant variations in the lift curves with simulated ice shape height. As the simulated ice shape height was increased from 0.10" to 0.25", the $C_{l,max}$ decreased from 0.60 to 0.27. Also, the angle of attack at which the lift curve diverged rapidly from the clean case decreased from 5° to 2°. Increasing the ice shape height increased drag at all angles of attack as Fig. 13b shows. Figure 13c shows that the simulated ice shape height had a significant effect on the pitching moment as well. As the ice shape was increased from 0.10" to 0.25", the angle of attack at which the pitching moment started to diverge rapidly from the clean case decrease from 5° to -1°. Increasing the ice shape size from 0.10" to 0.25" decreased the angle of attack at which the flap hinge moment diverged rapidly from the clean case from 6° to 1°.

The reason for this behavior is that as the simulated ice shape height was increased, the separation bubble was larger in chordwise extent. This can be seen in the surface pressure plots of Fig. 14. When the simulated ice shape was 0.10" high, the separation bubble reattached near x/c = 0.45. When the ice shape was 0.15" high, it was not clear where the reattachment location was because of the large effect on the flowfield. However, it appeared that the reattachment took place near x/c = 0.65 because downstream of this location, the C_p profile looked very similar to the clean case except for the 0.1 offset. When the simulated ice shape was 0.25" high, it was not clear if the separation bubble reattached on the model. If it had, it was most likely near the trailing edge. As the simulated ice shape

height was increased, the C_p in the separation bubble increased. A reduction in the suction peak upstream of the ice shape was also observed as the ice shape height was increased. The higher C_p values in the separation bubble and the smaller suction peak decreased the lift (from to 0.51 to 0.25 as the ice shape height was increased from 0.10" to 0.25" at $\alpha = 5°$). The longer separation bubble also resulted in earlier stall, higher drag, and an earlier divergence of the pitching and the flap-hinge moments from the clean values, as Fig. 13 shows.

Figure 15 shows the summary of the $C_{l,max}$ with the three simulated ice shape sizes at various x/c locations. Also shown in the figure is the summary of $C_{l,max}$ with the 16-grit roughness (k/c = 0.0014, density = 30%) as described in the Experimental Setup section. It shows that increasing the simulated ice shape height increased $C_{l,max}$ everywhere except at the leading edge. The simulated ice shape height did not have a large effect on $C_{l,max}$ at the leading edge, with the $C_{l,max}$ ranging from 0.92 to 1.01. In fact, the $C_{l,max}$ for the 0.15" simulated ice shape was higher than that of the 0.10" shape. Another interesting feature is that as the ice shape height was decreased from 0.25" to 0.10", the location of the minimum $C_{l,max}$ moved upstream from x/c = 0.12 to 0.10. This upstream movement of the minimum $C_{l,max}$ location with decreasing ice shape size is clearly evident in the roughness data. The 16-grit roughness had an average height of 0.025", making it approximately ¼ the height of the 0.10" simulated ice shape (the smallest one that was tested). The minimum $C_{l,max}$ for the roughness occurred when it was located at x/c = 0.02, and continued the trend of the simulated ice shapes. When the roughness was placed at the leading edge, the $C_{l,max}$ was 0.90, which was similar to what was observed for the ice shapes.

The upstream movement of the minimum $C_{l,max}$ location was probably due to the following reason. As the simulated ice shape size was decreased, the critical location became more sensitive to the location of the maximum local air velocity and less on the location of the maximum adverse pressure gradient. This occurred because the bubble length decreased as the ice-shape size decreased. Since the location of the maximum local velocity is closer to the leading edge than that of the maximum adverse pressure gradient, the ice-shape location with the lowest $C_{l,max}$ moved upstream as the ice shape size was decreased.

Effect of Simulated Ice Shape Geometry

The effects of the simulated ice shape geometry on airfoil aerodynamics were also studied in order to understand what the critical features were. Figure 16 shows the effect of various geometries (as shown in Fig. 3) on lift and flap hinge moments. All of the simulations shown in Fig. 16 had height of 0.25". Figure 16a shows that the forward facing quarter round had $C_{l,max}$ of 0.27 while the backward facing quarter round has a $C_{l,max}$ of 0.34. The backward facing quarter round had only a slightly less severe effect on lift than the forward facing quarter round even though the side facing the flow was much more streamlined. The half round had a significantly higher $C_{l,max}$ (0.58) than the backward facing quarter round even though they had an identical forward face exposed to the flow. Thus, the geometry of the downstream side had a significant effect on lift. However, this was the case only when the face exposed to the flow is streamlined (such as with the backward facing quarter round and the half round). Fig. 16a shows that the forward facing quarter round and the ramp shape had nearly identical lift curves even though they had very different downstream sides. Thus, for the two shapes with very blunt forward faces, the shape of the backward face was not as important (for the shapes tested).

Similar effects were observed for the flap hinge moments, as shown in Fig. 16b. It shows that the backward facing quarter round experienced C_h divergence at a higher α than the forward facing quarter round. The half round, in turn, had the divergence at a significantly higher α than the backward facing quarter round. Finally, the forward facing quarter round and the ramp shape had nearly identical flap hinge curves.

Effects of Roughness Near Ice Shape

SLD icing flight tests have shown the presence of roughness-type accretion upstream and downstream of the spanwise ice shape. Thus, it was important to understand the effect of the roughness-type accretion on the iced-airfoil aerodynamics. The roughness type accretion was simulated using 16-grit roughness tape extending upstream and downstream from the simulated ice shape (with k/c = 0.0014, density = 30%). The size and density of the roughness was identical to the roughness only case in Fig. 15. Figure 17 shows the result of the roughness on lift. In all of the cases, a 0.25" forward facing quarter round was used at x/c = 0.10. Unlike in the other cases, the boundary layer on the upper surface was not tripped. That is the reason why the no-roughness $C_{l,max}$ shown in Fig. 17 is 0.37 and the $C_{l,max}$ shown in Fig. 6a is 0.25. The various extents of the roughness that were tested did produce large relative changes in lift, but they were not large in an absolute sense since the C_l values were so low. Figure 17 shows that the lowest $C_{l,max}$ (0.31) resulted when the roughness extended 0.5" in front of the ice shape. When the chordwise roughness extent was 0.25", most or all of the roughness was located inside

the separation bubble that formed upstream of the ice shape, lessening its effect ($C_{l,max}$ = 0.34). When the roughness extent was increased from 0.5" to 2", the $C_{l,max}$ increased from 0.31 to 0.37. This may have happened because the roughness decreased the effective height of the ice shape by displacing the boundary layer upwards. Figure 17 also shows that when the 2" chordwise extent roughness was placed immediately downstream of the roughness in addition to the 1" extent upstream, the resulting $C_{l,max}$ was 0.32. This was slightly lower than the case with only the 1" extent upstream roughness ($C_{l,max}$ = 0.34). Thus the roughness downstream of the ice shape had a measurable effect on lift even though it was completely submerged within the long separation bubble that formed downstream of the ice shape.

CONCLUSION

An experimental study was conducted in order to understand the effects of spanwise-step ice accretion on aircraft aerodynamics. The following conclusions can be drawn based on the results.

1. Large differences in aerodynamics characteristics were observed between the NACA 23012 and NLF 0414 airfoils with spanwise-step ice simulations.

2. The effects of the ice shape simulation were much more severe on the NACA 23012. With the 0.25" (k/c = 0.0139) ice shape simulation, the lowest $C_{l,max}$ on the NACA 23012 was 0.25. On the NLF 0414 the lowest $C_{l,max}$ was 0.68.

3. The most critical ice shape location (in terms of lift loss) for the NACA 23012 was near x/c = 0.12. On the NLF 0414, the $C_{l,max}$ did not vary by a large amount when the simulated ice shape was located between x/c = 0.02 and 0.20.

4. On the NACA 23012, the largest increase in drag occurred when the simulated ice shape was located at the location of the maximum local air velocity of the clean model. This did not occur for the NLF 0414.

5. The largest loss in lift on the NACA 23012 occurred when the simulated ice shape was located in the region between the largest local air velocity and the maximum adverse pressure gradient of the clean model. Again, this did not occur for the NLF 0414.

6. The ice shape affected C_h much more on the NACA 23012 than on the NLF 0414. On the clean NACA 23012, the flap is lightly loaded. When the separation bubble due to the ice shape reached the flap, the flap became heavily loaded and caused a large change in the $C_{h,\alpha}$ slope. On the NLF 0414, the flap was heavily loaded even on the clean model due to early flap separation. Thus, even when the bubble reached the flap, it did not significantly alter the C_h at $\alpha > 5°$.

7. The differences described above were due to large differences in the clean model pressure distribution between the NACA 23012 and the NLF 0414. The NACA 23012 is a very front loaded airfoil, with a very large leading edge suction peak. The NLF 0414 has relatively uniform chordwise loading until the pressure recovery near the trailing edge. On the NACA 23012, the largest penalties occurred when the simulated ice shape prevented the leading-edge suction peak from forming. On the NLF 0414, the largest aerodynamic penalties occurred when the simulation ice shape (and the associated separation bubble) was located near the trailing-edge pressure recovery region.

8. On the NACA 23012 the simulated ice shape location at which the lowest $C_{l,max}$ occurred moved upstream with decreasing ice shape size.

9. The variations in the geometry of the ice shape simulation had some effect on airfoil aerodynamics, with the half-round shape having a significantly higher $C_{l,max}$.

10. The presence of roughness immediately upstream of the ice shape had measurable (although not large) effects on airfoil aerodynamics. The presence of roughness downstream of the ice shape did not have any significant effect.

ACKNOWLEDGEMENTS

This work was supported by the Federal Aviation Administration (FAA) under grant DTFA MB 96-6-023 with Dr. James Riley as technical monitor. The authors would also like to thank Mr. Gene Hill from FAA, Mr. Tom Bond and Dr. Mark Potapczuk from NASA, and Prof. Eric Loth, Mr. Tim Dunn, and Mr. Satish Kumar from the University of Illinois at Urbana-Champaign for their contribution to this research.

REFERENCES

[1] National Transportation Safety Board, "Icing Tanker Test Factual Report," Docket No: SA-512, Exhibit No: 13B, DCA95MA001, Washington D.C., Feb. 16, 1995.

[2] Dow Sr., John P., "Roll Upset in Severe Icing," Federal Aviation Administration - Aircraft Certification Service, September 1995.

[3] Ashenden, R. and Marwitz, J., "Turboprop Aircraft Performance Response To Various Environmental Conditions," AIAA Paper 97-0305, *Journal of Aircraft*, Vol 34, no. 3, May-June 1997, pp. 278-287.

[4] Ashenden, R., Lindberg, W. and Marwitz, J., "Two-Dimensional NACA 23012 Airfoil Performance Degradation by Super Cooled Cloud, Drizzle, and Rain Drop Icing," AIAA 34th Aerospace Sciences Meeting, Reno, NV, January 15-18, 1996.

[5] Bragg, M.B., "Aircraft Aerodynamic Effects Due To Large Droplet Ice Accretions," Paper No. 96-0932, AIAA 34th Aerospace Sciences Meeting, Reno, NV, January 15-18, 1996.

[6] Bragg, M.B., "Aerodynamics of Supercooled-Large-Droplet Ice Accretion and the Effect on Aircraft Control," *Proceedings of the FAA International Conference on Aircraft Inflight Icing*, Volume II, DOT/FAA/AR-96/81,II, August 1996, pp. 387-399.

[7] Jacobs, E. N., "Airfoil Section Characteristics as Affected by Protuberances," NACA Report No. 446, 1932.

[8] Bowden, D.T., "Effect of Pneumatic De-Icers and Ice Formations on Aerodynamic Character of an Airfoil," NACA Technical Note 3564, February, 1956.

[9] Calay, R.K., Holdù, A.E. and Mayman, P., "Experimental Simulation of Runback Ice," *Journal of Aircraft*, Vol. 34, No, 2, March - April, 1997, pp. 206-212.

[10] Lee, S., Dunn, T., Gurbacki, H.M., Bragg, M.B., and Loth, E., "An Experimental and Computational Investigation of Spanwise-Step-Ice Shapes on Airfoil Aerodynamics," AIAA Paper 98-0490, 36th Aerospaces Sciences Meeting & Exhibit, Reno, NV 1998.

[11] Dunn, T. and Loth, E., "Effects of Simulated-Spanwise-Ice Shapes on Airfoils: Computational Investigation," AIAA Paper 99-0093, 37th Aerospace Sciences Meeting & Exhibit, Reno, NV 1999.

[12] Rae, W. H. and Pope, A., *Low-Speed Wind Tunnel Testing*, John Wiley & Sons, 1984.

[13] Althaus, D. and Wortmann, F. "Experimental Results from the Laminar Wind Tunnel of the Institute for Aerodynamic and Gasdynamics - The University of Stuttgart" published by Princeton University, Department of Mechanical and Aerospace Engineering, 1979.

[14] Gregory, N. and O'Reilly, C.L., "Low-Speed Aerodynamic Characteristics of NACA 0012 Aerofoil Section, including the Effects of Upper-Surface Roughness Simulating Hoar Frost," ARC R&M 3726, Jan. 1970.

[15] Tani, I., "Low Speed Flows Involving Bubble Separations," Progress in Aeronautical Sciences, Pergamon, New York, 1964, pp. 70-103.

Table 1. Experimental uncertainties for the clean NACA 23012 model at $\alpha = 5^{o}$. Re = 1.8 million.

Aerodynamic Coefficient	Reference Value	Absolute Uncertainty	Relative Uncertainty
C_l Pressure	0.633	2.11×10^{-03}	0.33%
C_d Wake	0.01022	1.43×10^{-04}	1.40%
C_m Pressure	-0.00894	3.49×10^{-04}	3.90%
C_h Balance	-0.0157	3.55×10^{-03}	9.70%

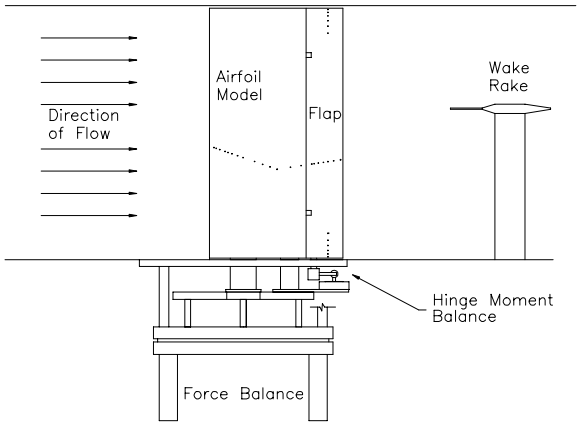

Fig. 1. Schematic of the experimental setup.

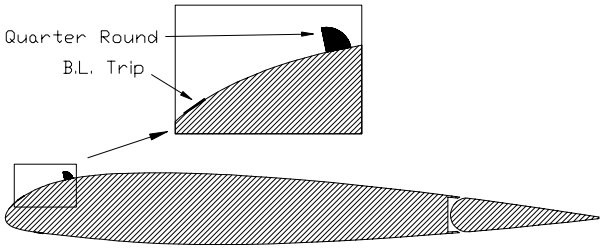

Fig. 2. NACA 23012 model with quarter round ice simulation. (0.25" quarter round at x/c = 0.10 shown)

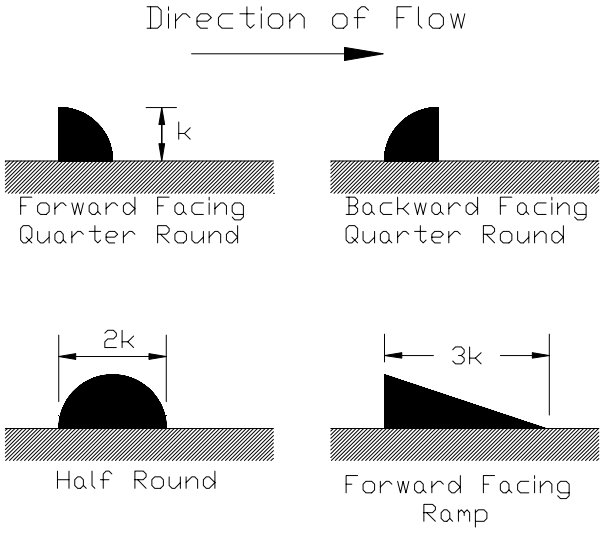

Fig. 3. Ice shape simulation geometry.

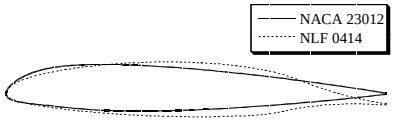

Fig. 4. Comparison between NACA 23012 and NLF 0414 geometry.

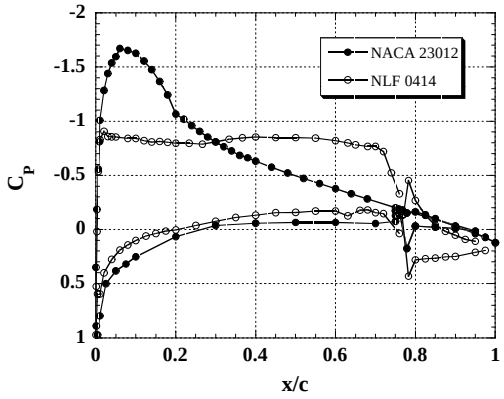

Fig. 5. Comparisons of clean model surface pressure distribution between NACA 23012 and NLF 0414. Re = 1.8×10^6. (NACA: 23012. $\alpha = 5.15°$, $C_l = 0.62$) (NLF 0414: $\alpha = 1.06°$, $C_l = 0.60$)

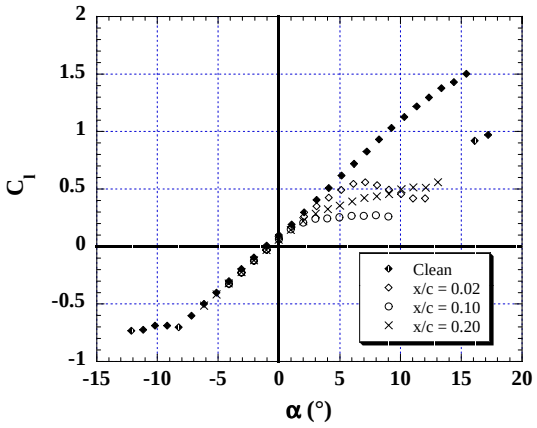

6a) NACA 23012

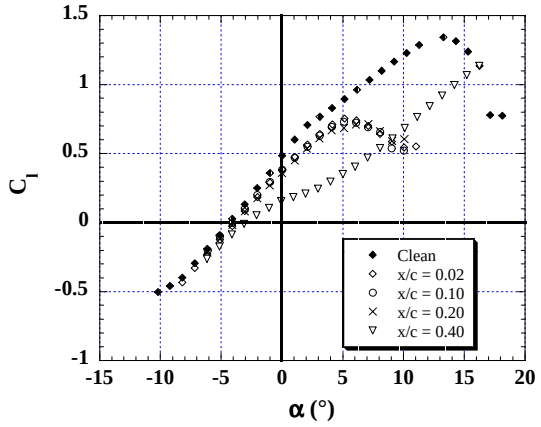

6b) NLF 0414

Fig. 6. Effect of simulated ice-shape location on lift. 0.25" forward facing quarter round; Re = 1.8×10^6; Boundary layer tripped.

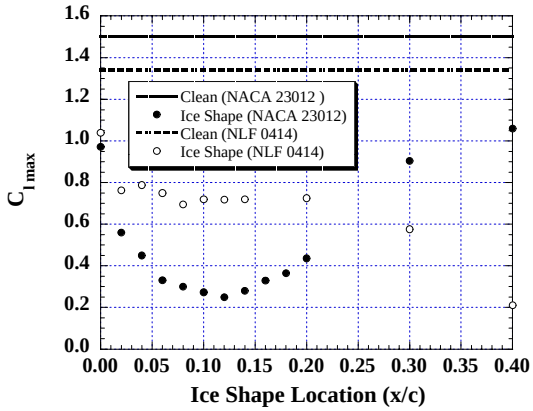

Fig. 7. Summary of $C_{l,max}$ with 0.25" forward-facing quarter round simulated ice shape at various chordwise locations.

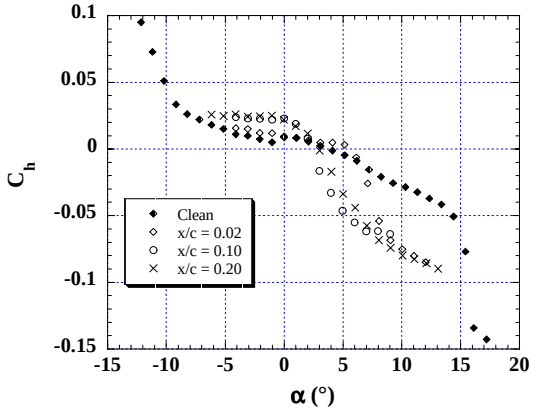

8a) NACA 23012

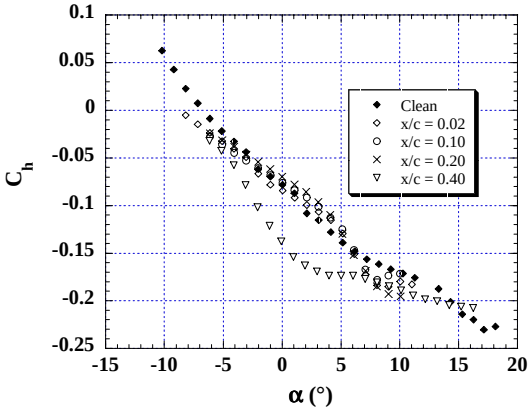

8b) NLF 0414

Fig. 8. Effect of simulated ice-shape location on flap hinge moment. 0.25" forward-facing quarter round; Re = 1.8×10^6; Boundary layer tripped.

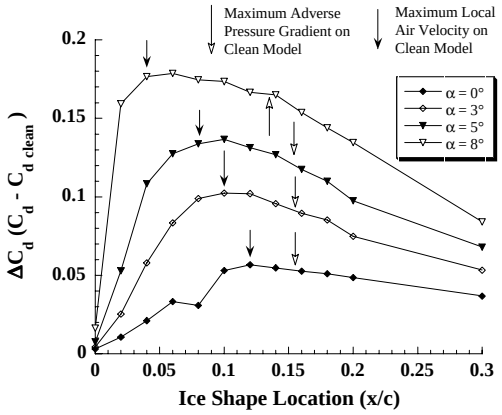

9a) NACA 23012

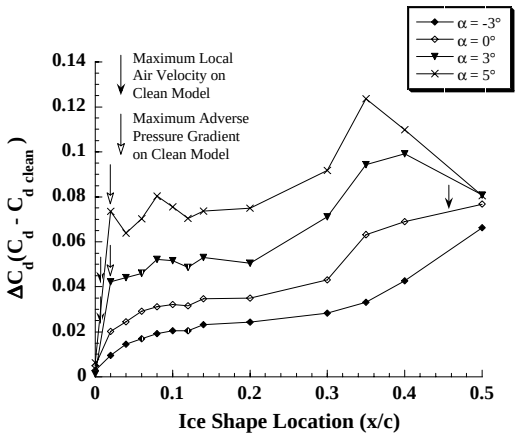

9b) NLF 0414

Fig. 9. Drag increase due to ice shape. 0.25" forward facing quarter round; Re = 1.8×10^6; Boundary layer tripped.

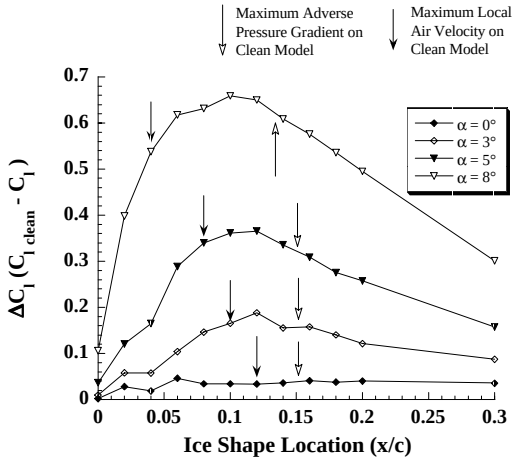

10a) NACA 23012

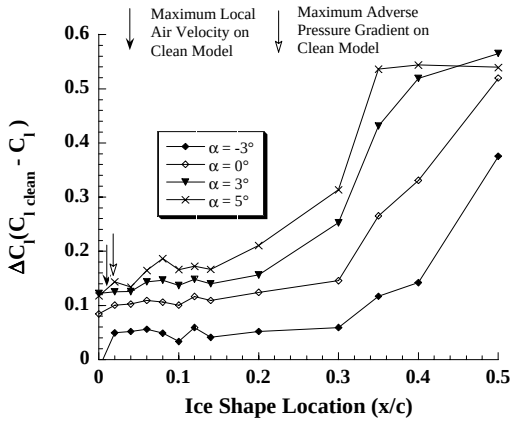

10b) NLF 0414

Fig. 10. Lift loss due to ice shape. 0.25" forward facing quarter round; Re = 1.8×10^6; Boundary layer tripped.

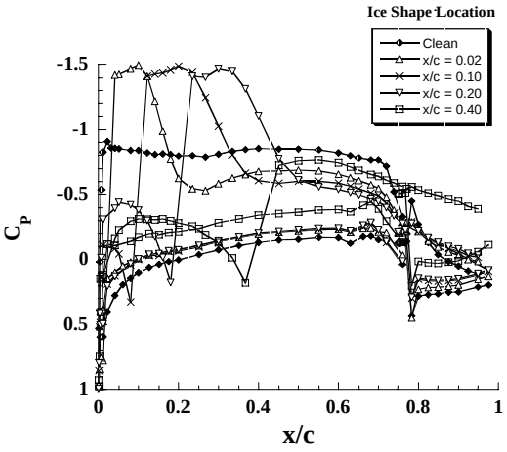

11b) NLF 0414, $\alpha = 1°$

Fig. 11. Effect of simulated ice shape location on surface pressure. 0.25" forward facing quarter round; $\alpha = 1°$; Re = 1.8×10^6; Boundary layer tripped.

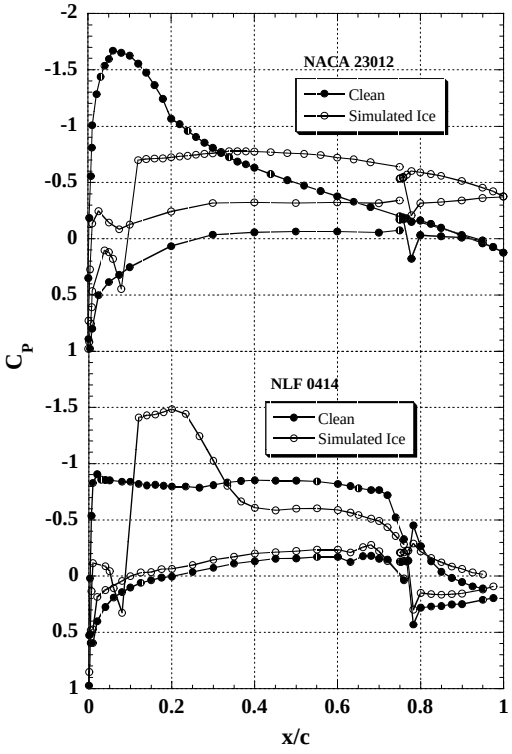

Fig. 12. Surface pressure comparisons between NACA 23012 and NLF 0414 with 0.25" ice shape simulation at x/c = 0.10. Re = 1.8×10^6; (NACA 23012: $\alpha = 4.93°$, $C_l = 0.25$) (NLF 0414: $\alpha = 1.06°$, $C_l = 0.47$)

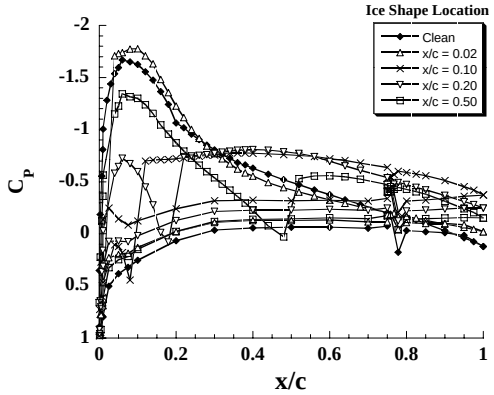

11a) NACA 23012, $\alpha = 5°$

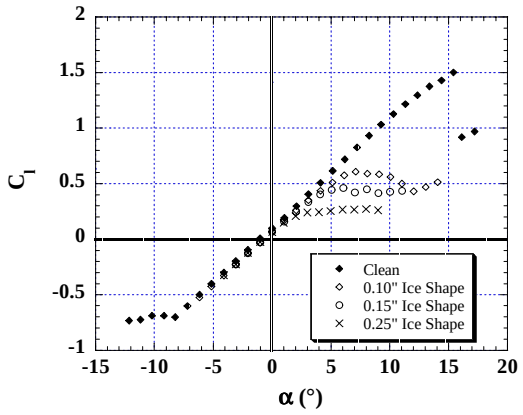

13a) C_l vs. α

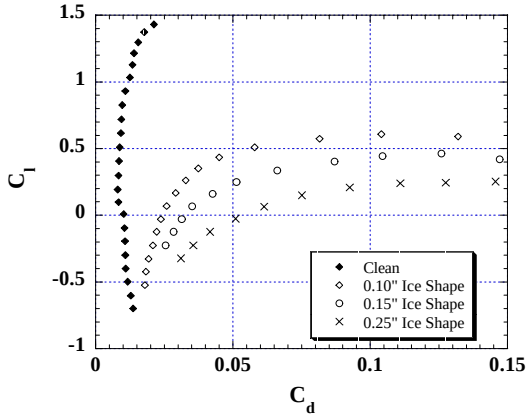

13b) C_l vs. C_d

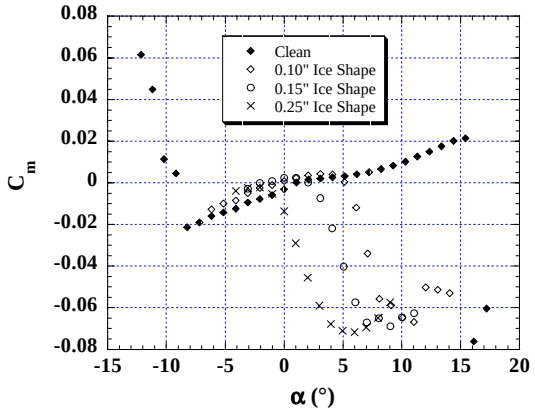

13c) C_m vs.α

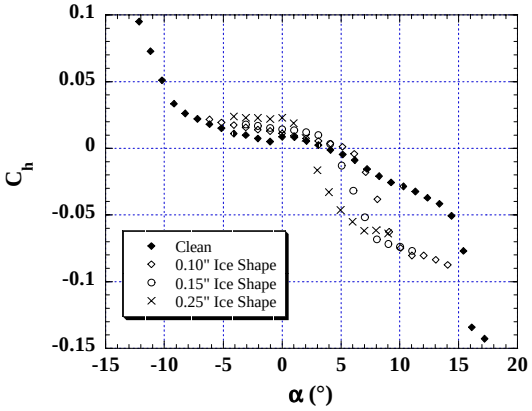

13d) C_h vs.α

Fig. 13. Effect of simulated ice-shape height on integrated aerodynamic coefficients. Forward facing quarter round; Re = 1.8×10^6; NACA 23012; Boundary layer tripped.

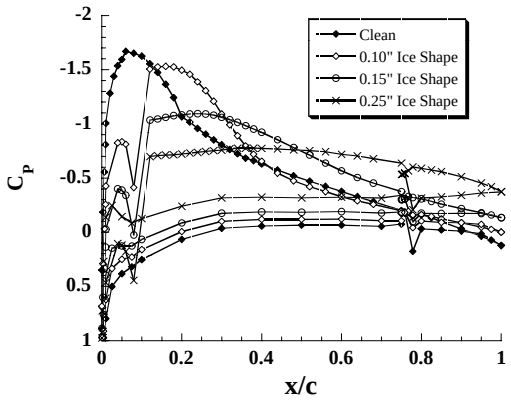

Fig. 14. Surface pressure with simulated ice shapes at x/c = 0.10. NACA 23012; Re = 1.8×10^6; Forward facing quarter round; Boundary layer tripped.

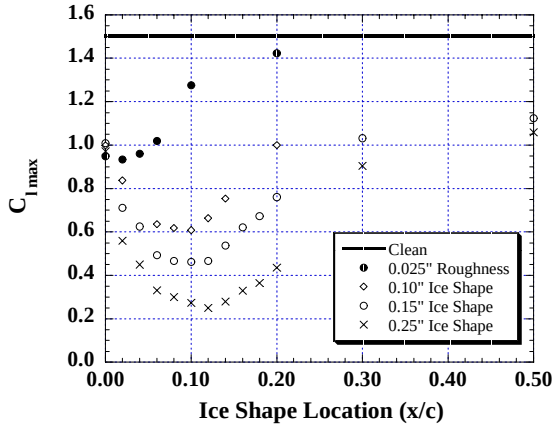

Fig. 15. Summary of $C_{l,max}$ with simulated ice shape at various chordwise locations. Forward facing quarter round; 16-grit roughness of ¼" chordwise extent; Boundary layer tripped; NACA 23012.

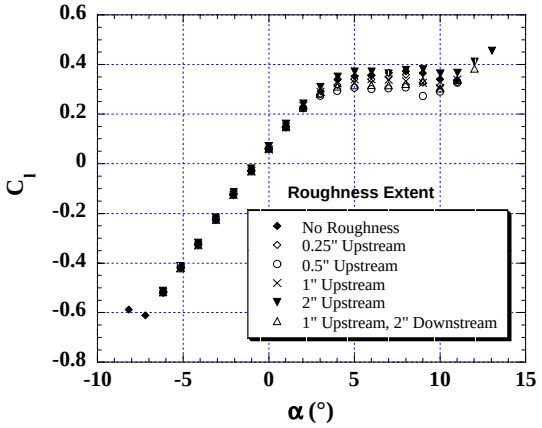

Fig. 17. Effect of roughness extent upstream and downstream of simulated ice shape on lift. 0.25" forward facing quarter round simulation at x/c = 0.10; 16-grit roughness

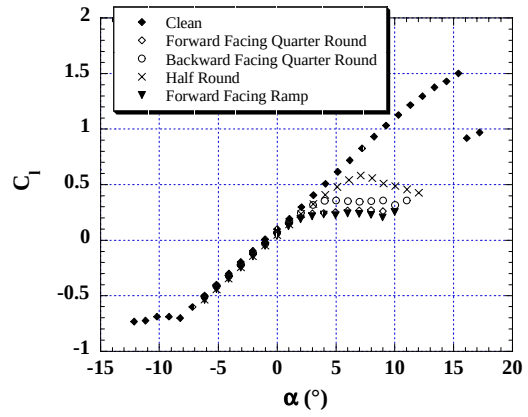

16a) C_l vs. α

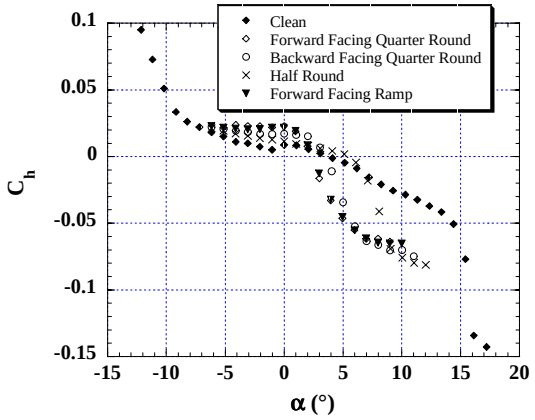

16b) C_h vs.α

Fig. 16. Effect of simulated ice-shape geometry on lift and flap-hinge moment. 0.25" simulation height; Re = $1.8x10^6$; Boundary layer tripped.